



ELSEVIER

Available online at www.sciencedirect.com

SCIENCE @ DIRECT®

Nuclear Instruments and Methods in Physics Research A 510 (2003) 176–184

**NUCLEAR
INSTRUMENTS
& METHODS
IN PHYSICS
RESEARCH**
Section Awww.elsevier.com/locate/nima

A photoelectric polarimeter based on a Micropattern Gas Detector for X-ray astronomy

R. Bellazzini^{a,*}, L. Baldini^a, A. Brez^a, E. Costa^b, L. Latronico^a,
N. Omodei^a, P. Soffitta^b, G. Spandre^a

^aINFN-Sezione di Pisa, University of Pisa, Via Buonarroti 2, 56100 Pisa, Italy

^bIstituto di Astrofisica Spaziale del CNR, V. Fosso del Cavaliere 100, 00133 Roma, Italy

Abstract

Polarimetry of cosmic X-rays is one of the possible observational approaches, together with spectroscopy, photometry and imaging, to study celestial sources. It can provide a general tool to explore the structure of compact sources and derive information on mass and angular momentum of supermassive objects. Comparing with the other three modalities, the development of X-ray polarimetry is modest, due to the inefficiency of traditional X-ray polarimeters. In this paper a new instrument (the Micropattern Gas Detector) to measure the linear polarization of X-ray sources with high efficiency is presented. It is based on the photoelectric effect. Angle and amount of polarization is computed from the angular distribution of the photoelectron tracks, reconstructed by a finely segmented gas detector. The device has pixel read-out allowing a full 2-D image reconstruction. The improvement in sensitivity is nearly two orders of magnitude with respect to traditional polarimeters. At the focus of a large X-ray telescope, in orbit, it can detect low level of polarization in galactic and extragalactic sources.

© 2003 Elsevier B.V. All rights reserved.

Keywords: X-ray; Polarimetry; Astrophysics; Micropattern Gas Detectors

1. Introduction

Theoretical models, in high-energy astrophysics, suggest that non-thermal emission mechanisms, scattering of radiation through highly asymmetric systems or vacuum polarization and birefringence in intense magnetic field can produce a high degree of linear polarization of X-ray radiation [1–4]. Expectations from polarimetric measurements for

astrophysical sources such as Neutron Stars, Galactic and Extragalactic Black Holes, X-ray Binaries and AGN, are very attractive. Unfortunately, conventional techniques based on Bragg diffraction at 45° or Compton scattering around 90° are poorly efficient and the only accepted measurement of X-ray polarization dates more than 25 years ago. It refers to the observation of the Crab Nebula with a Bragg crystal polarimeter flown on board of the satellite OSO-8 [5].

Fig. 1 shows the X-ray image of the center of the Crab, the blastwave of a Supernova with a bright pulsar in its core, obtained with the Chandra X-ray Observatory. A torus of radiation is visible

*Corresponding author. Tel.: +39-050-221-4367; fax: +39-050-221-4317.

E-mail address: ronaldo.bellazzini@pi.infn.it
(R. Bellazzini).

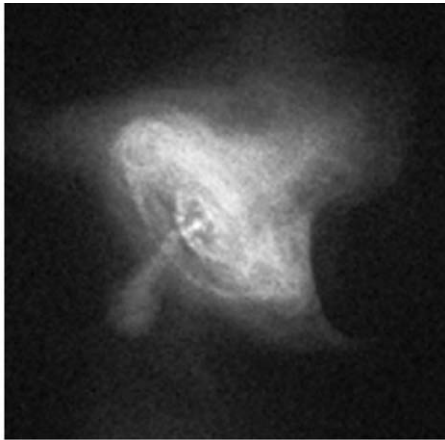


Fig. 1. Polarization of SNR: the Crab Nebula seen by the Chandra X-ray Observatory.

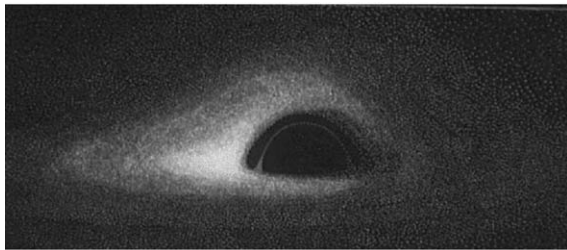


Fig. 2. Simulated view of accretion disk around a BH. Light bending makes visible the bottom part of the disk. Doppler boosting produces an increase of the intensity on one side.

around the pulsar with two jets emerging from the poles. High-energy electrons caught by an intense magnetic field emit polarized synchrotron radiation. The Crab Nebula has same degree and angle of polarization from radio to X-ray, a clear signature of synchrotron emission.

Unlike spectral data, polarization data are strongly affected by general relativistic effects. In a BH, surrounded by an optically thick and geometrically thin accretion disk, higher energy photons come from the smaller disk radii. As the photon energy increases from 1 to 10 keV, the plane of linear polarization will swing smoothly through an angle of $\sim 27^\circ$ for a 9 Solar Mass BH and $\sim 40^\circ$ for an extreme Kerr BH (for an inclination of 41°).

This effect is due to the strong gravitational bending of light rays (Fig. 2). In this paper a new

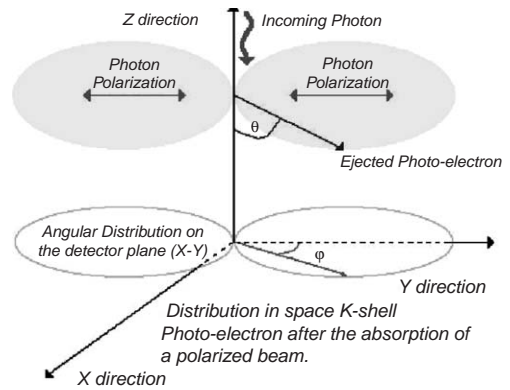


Fig. 3. Angular distribution on the detector plane (XY) of the ejected photoelectrons.

polarimeter based on the photoelectric effect is described. The instrument is highly efficient in the energy range 2–10 keV, particularly interesting for X-ray Astronomy.

2. The Micropattern Gas Detector

The photoelectric effect is a process very sensitive to photon polarization and with a large cross-section at low energy. In the case of linearly polarized photons, the differential photoelectron cross-section has a maximum in the plane orthogonal to the direction of the incoming photon:

$$\frac{d\sigma}{d\Omega} = r_0^2 Z^5 \alpha^4 \left(\frac{m_e c^2}{h\nu} \right)^{7/2} \frac{4\sqrt{2} \sin^2 \theta \cos^2 \phi}{(1 - \beta \cos \theta)^4} \quad (1)$$

θ is the polar and ϕ the azimuthal angle (Fig. 3).

The photoelectron is ejected with maximum probability in the direction of the photon electric field with a $\cos^2 \phi$ modulation. Fig. 4 shows the principle of operation of the Micropattern Gas Detector, developed to efficiently track the photoelectron [6].

After the absorption of the photon in the gas volume, the ejected photoelectron produces a track of ion–electron pairs. Ions and electrons are separated by the applied electric field and the electrons drift towards an amplifying grid (the Gas Electron Multiplier). The amplified charge is then collected by read-out pixels (Fig. 5) individually

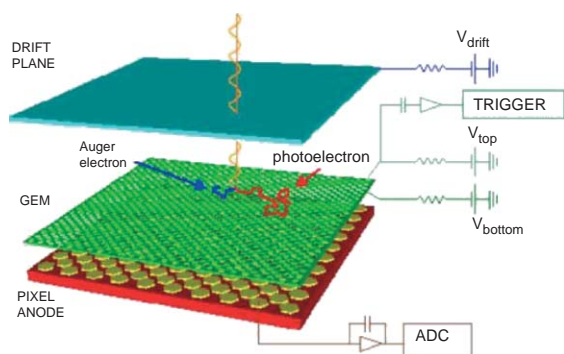


Fig. 4. The Micropattern Gas Detector. Read-out plane is grounded, while both sides of the GEM and the drift plane are at increasingly negative high voltage.

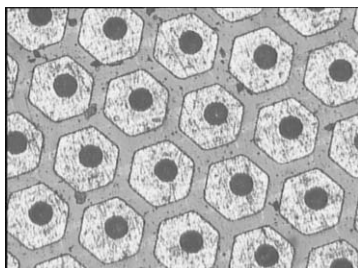


Fig. 5. Microscope picture of the hexagonal pixels of the read-out plane.

connected to independent analog electronic channels. The output signal is proportional to the charge collected by the pixel; the track image contains also information on the dynamics of the photoelectron energy loss. The multi pixel read-out plane allows a real two-dimensional reconstruction. Being of the order of 1 mm, the photoelectron track is well sampled by pixels at 200 μm pitch and the track reconstructed with very good resolution.

In the initial part of the track, where the ionizing process dominates with respect to the scattering process, resides the information on the original electron direction and thence the key to derive the polarization of the photon.

This dependence is preserved when the track is projected onto a plane perpendicular to the direction of the incoming radiation, as in this case. The GEM (Fig. 6) consists of a thin (50 μm) insulating foil, metalized on each side and etched

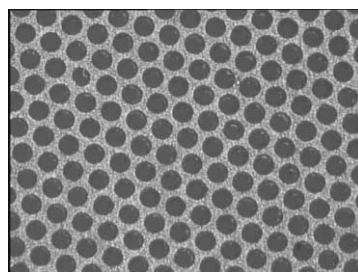


Fig. 6. Microscope picture of the GEM structure.

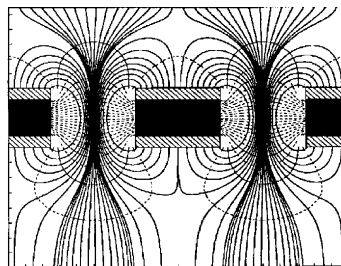


Fig. 7. The electric field structure in the GEM. High transfer.

with a regular pattern of holes (60 μm in diameter, 90 μm pitch). A suitable electric field applied between the two sides of the GEM creates a very intense dipole field inside the holes to induce avalanche electron multiplication. Higher transfer efficiency is provided by the focusing–defocusing effect of the electric field (Fig. 7). The GEM gives also the trigger signal to read-out electronics.

The MPGD is filled with a gas mixture of Neon (80%)—dimethylether (20%) at 1 atm pressure. The choice of the gas mixture is critical to get high efficiency, which increases with Z , and good track reconstruction, which conversely decreases with increasing Z .

A low Z gas mixture has been chosen for its high stopping power/scattering ratio and a still reasonable detection efficiency. Moreover, due to the low energy K-edge of Neon, Auger electrons, emitted isotropically, will get only a small fraction of the photon energy so that they will not blur the directional information. Finally, in low Z gas, tracks are longer so angular reconstruction is easier. Fig. 8 shows the read-out pixel plane of the MPGD with the relative electronics. The GEM and the drift plane are then glued with two

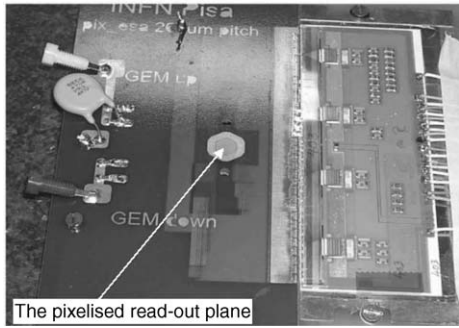


Fig. 8. The multi-pixels read-out plane. Pixels are 512 at 200 μm pitch.

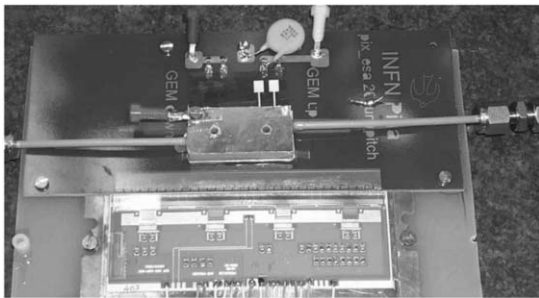


Fig. 9. The overall detector assembly and read-out electronics.

fiberglass spacers, respectively, of 1.5 mm (transfer gap) and 6 mm (absorption gap) over the read-out plane (Fig. 9).

3. Results

The MPGD has been tested with unpolarized (5.9 keV from a ^{55}Fe source) and polarized radiation. Polarized X-rays have been obtained by Thompson scattering on a Li target of photons produced by an X-ray tube with Cu (8.04 keV) or Cr (5.4 keV) anode. A double diaphragm collimator limited the scattering angles to $90^\circ \pm 5^\circ$. In this way the radiation is linearly polarized at 98%. A sample of real photoelectron tracks obtained with the MPGD is shown in Fig. 10.

Ionization density is not uniform and the end of the track is characterized by a larger release of charge.

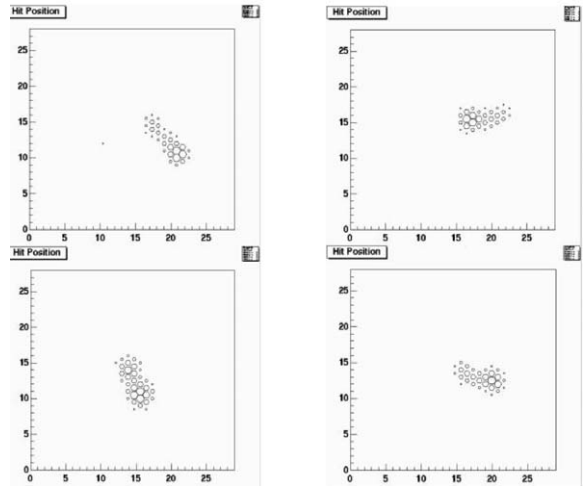


Fig. 10. Real tracks of photoelectrons from 5.9 keV unpolarized photons. The area of each hexagon is proportional to the charge collected by the corresponding pixel.

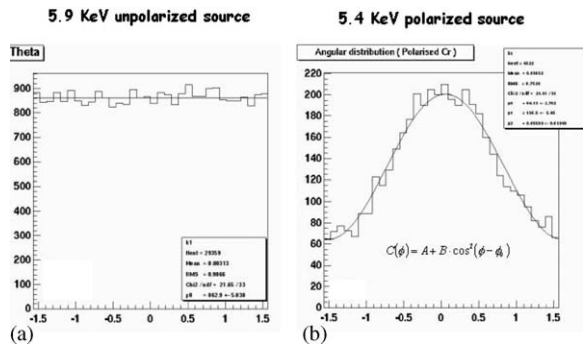


Fig. 11. Cluster angular distribution for unpolarized (a) and polarized radiation (b).

The direction of emission of the photoelectron is reconstructed in first approximation by finding the principal axes of the charge distribution on the pixels. These two orthogonal directions provide the maximum and minimum second momentum of the charge distribution, with respect to the barycenter. The major principal axis is identified as the photoemission direction.

Fig. 11 shows the angular distribution of the tracks for unpolarized and polarized radiation. In the unpolarized case, as expected, the distribution is flat, while in other case it is peaked around the polarization angle and modulated according to

the function:

$$C(\phi) = A + B \cos^2(\phi - \phi_{\text{pol}}). \quad (2)$$

The constant term is due to the randomization induced by Coulomb scattering while the \cos^2 term derives from the cross-section of the photoelectric effect. A fundamental parameter in polarimetry is the so-called *modulation factor*. For 100% linearly polarized radiation, it results from Eq. (2) as follows:

$$\mu = \frac{C_{\text{max}} - C_{\text{min}}}{C_{\text{max}} + C_{\text{min}}} = \frac{B}{2A + B}. \quad (3)$$

The distribution of Fig. 11b has a modulation factor of $\sim 50\%$.

At a higher level of approximation, a better reconstruction of the photoemission angle is possible by evaluating the absorption point (or impact point) identified, in the first pass algorithm, with the barycenter. In asymmetric charge distributions, the third momentum (M_3) lies along the major axis on the side, with respect to the barycenter, where the charge release is smaller. Since the ionization density is lower at the beginning of the track, this approach allows one to estimate the location of the absorption point, which is a reference point much more accurate than the barycenter.

This point is obtained going back from the barycenter, along the major axis on the direction of M_3 , of a distance L such as

$$L = f \sqrt{M_2^{\text{max}}} \quad (4)$$

where $f \approx 1$ is tuned on data using MC simulation.

A new cluster of pixels, whose distance from the impact point is less than a set threshold, is defined and new principal axes are computed. The result of this algorithm applied to a photoelectron track seriously affected by Coulomb scattering is shown in Fig. 12.

In Fig. 13 the dependence of the modulation factor with the track length used in the reconstruction is shown. In the *re-defined* clusters, new barycenters with respect to the absorption point are computed. The distribution of these barycenters is shown in Fig. 14 both for unpolarized (left panel) and polarized radiation (right panel). The distribution on the right is clearly asymmetric,

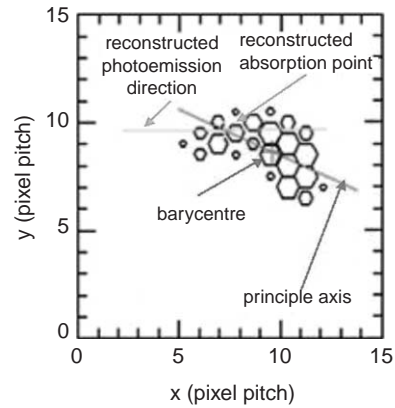


Fig. 12. Real photoelectron track. Reconstruction of the photoemission direction is done with the identification of the absorption point and the removal of the final part of the track.

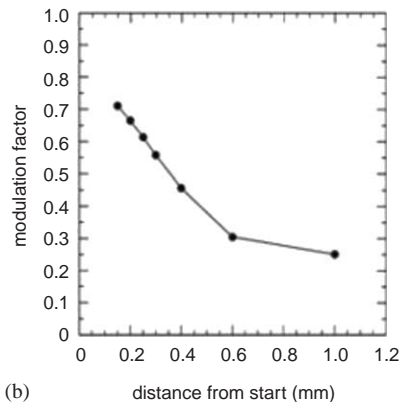


Fig. 13. Modulation factor as a function of the track length used in the reconstruction. The plot refers to 5 keV simulated photoelectrons in 1 atm pure Neon.

reflecting the preferential direction of emission of the photoelectron.

In Fig. 15 the distributions of both barycenters and absorption points are shown for comparison. The plots refer to collimated unpolarized radiation. The collimator diameter is only $50 \mu\text{m}$, much smaller than pixel size thus the absorption points are concentrated in a very small spot $70 \mu\text{m}$ (rms) in diameter. Barycenters are instead distributed at some distance from the absorption points because of the large energy release at the end of the track.

The imaging capability of the MPGD has been also tested. Fig. 16 shows the bi-dimensional plots of barycenters (left) and impact points (right) of

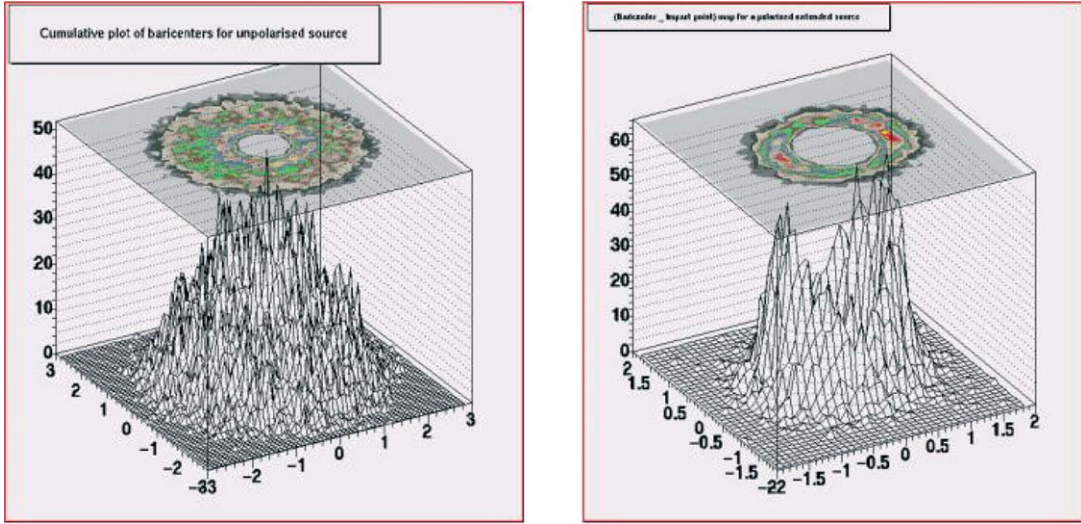


Fig. 14. Distribution of the track barycenters with respect to the absorption point for 5.9 keV unpolarized (left) and 5.4 keV polarized radiation (right).

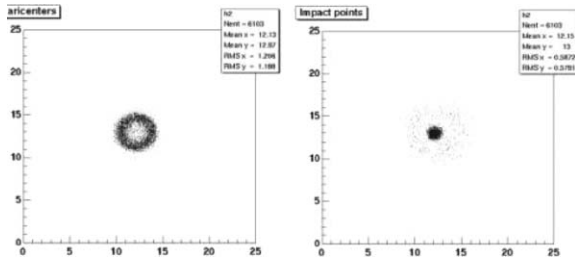


Fig. 15. Distribution of barycenter (left) and absorption points (right) of a collimated unpolarized radiation (5.4 keV). Events with clusters shape asymmetry ($= M_2^{\max}/M_2^{\min}$) > 2.5 are selected.

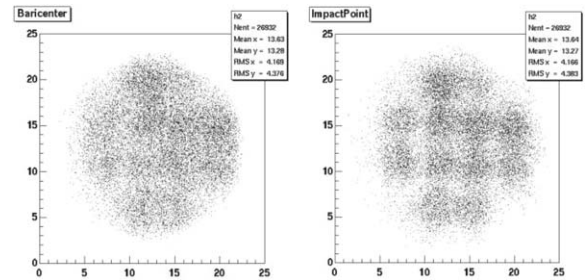


Fig. 16. 2D-image obtained with reconstructed barycenters (left) and impact points (right). In the left plot the pattern of the collimator used is clearly visible.

the clusters produced in the detector by X-ray radiation passing through a pattern of holes, 500 μm in diameter and 1 mm pitch.

The sensitivity of a polarimeter is usually defined in terms of Minimum Detectable Polarization (MDP) which is the minimum modulated flux needed to exceed, at a defined level of confidence, the statistical fluctuations of both the background and the unmodulated signal (the unpolarized fraction of the source). At n standard deviations MDP is [7] is given by

$$\text{MDP}(n_\sigma) = \frac{n_\sigma}{\varepsilon\mu F} \sqrt{\frac{2(B + \varepsilon F)}{ST}} \quad (5)$$

where F is the source flux, B the background rate, S the collecting area, T the observing time, ε the detection efficiency. Eq. (5) allows evaluating the time necessary to perform a planned measurement. Moreover, in the case of negligible background with respect to the source flux, which is the case of a polarimeter at the focus of an X-ray optics, the MDP becomes

$$\text{MDP} \propto \frac{1}{\mu\sqrt{\varepsilon}} \text{(for bright sources)}. \quad (6)$$

Conversely for faint sources it results:

$$\text{MDP} = \frac{1}{\sqrt{\mu\varepsilon}}. \quad (7)$$

The modulation factor, as well as the flux, background, efficiency and effective area, are quantities which depend on energy. A complete MonteCarlo simulation that takes into account the full process from the absorption of photons in the active volume, the photoelectrons emission, the interaction of the photoelectrons in the gas

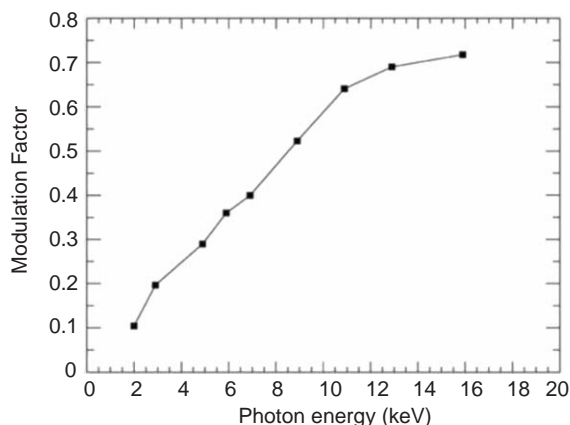


Fig. 17. Simulated modulation factor as a function of the photon energy. No event selection is applied. Conditions are slightly different from the prototype described in the paper: gas mixture is Ne/DME 80/20, absorption gap 1 mm and read-out pitch 100 μm .

mixture, the diffusion of the primary ionization, the avalanche multiplication in the GEM and the collection of the charge on the read-out plane, has been developed. The MC has been tuned with real data. Results from the simulation are in very good agreement with experimental data. In Fig. 17 the dependence of the modulation factor with the photon energy, obtained with the MC simulation, is plotted. With the present MPGD prototype at the focus of Sodart X-ray optics, a gain of a factor 5, in terms of integration time, over Bragg and Thompson techniques exploited by SXP (Stellar X-ray Polarimeter) is easily achievable. Table 1 shows the performance evaluated for the actual prototype and for an optimized configuration, at the focus of Sodart.

To further increase detection efficiency, the optimized MPGD has a thicker gas gap (30 mm) and operates at higher pressure (4 atm). These parameters will increase efficiency up to $\sim 90\%$ but track reconstruction capability strongly decreases being tracks too short. For this reason the read-out pitch should be reduced to 50 μm implying a huge number of pixels (up to 40000). In these conditions the actual PCB technology cannot be adopted. VLSI read-out plane with integrated electronics is the only possible solution.

Table 1
Present and optimized configuration of a MPGD for astrophysical applications

	Present prototype (2–10 keV)	Improved configuration (3.5–10 keV)
Drift/absorption gap	6 mm	30 mm
Drift field	3000 V/cm	1500 V/cm
Gas filling and pressure	(Ne 80% DME 20%) 1 atm	(Ne 40% DME 60%) 4 atm
Gas gain	5000	2500
Transverse diffusion in drift	80 μm	< 100 μm
GEM thickness	50 μm copper clad Kapton foil	50 μm copper clad Kapton foil
GEM hole geometry	40 μm diameter, 60 μm pitch	40 μm diameter, 60 μm pitch
GEM voltage	400 V	600 V
Detection efficiency at 5.4 keV	3.8%	91%
Read-out pixel size	200 μm	50 μm
No of pixels	512	40000
Read-out plane technology	Multilayer advanced PCB	VLSI
Track length/pixel size at 6 keV	6	6
Sensitivity to Her X1	$T = 400$ s; MDP 10%	$T = 22$ s; MDP 10%
Sensitivity to 3C-273	$T = 2.2 \times 10^5$ s; MDP 2%	$T = 4 \times 10^4$ s; MDP 1%
Sensitivity to MCG-6-30-15	$T = 5 \times 10^5$ s; MDP 2%	$T = 1 \times 10^5$ s; MDP 10%
Gain in the integration time over SXP (strong source)	5 over Thomson, 15 over Bragg	100 over Thomson, 2000 over Bragg
Gain in the integration time over SXP (faint source)	200 over Thomson, 100 over Bragg	5000 over Thomson, 2000 over Bragg



Fig. 18. The XEUS space observatory.

Table 2

MDP for AGNs in the 2–10 keV energy band for 10^5 s observation with the existing MPGD prototype at the focus

AGN	MDP %
CENA	0.6
NGC4151	0.7
NGC5548	0.8
MGC6-30-15	1.2
Circinus Galaxy	2.8
IC4329A	0.7
Fairall 9	1.6
MKN501 (outburst)	0.5
MKN421	0.7
3C273	0.9

Actually similar VLSI pixel chips for digital X-ray cameras are commercially available. The capabilities of the present prototype, in particular the position resolution of about $70 \mu\text{m}$, can be optimally exploited at the focus of XEUS-1.

The X-ray Evolving Universe Spectroscopy mission (XEUS [8]) will be a permanent space-born X-ray observatory. It will consist of a Detector spacecraft with the focal plane instrumentation that receives cosmic X-rays focused by a Mirror spacecraft flying at 50 m in front of it (Fig. 18).

The existing MPGD could perform polarimetry at the % level on many bright AGN in about 1 day observation, in the energy range 2–10 keV (Table 2). Much more detailed study would be possible on Galactic Sources.

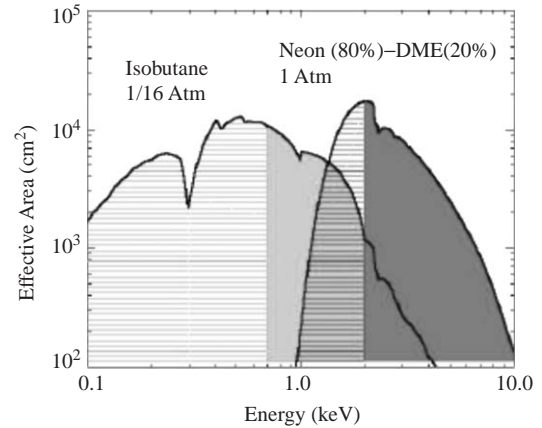


Fig. 19. Effective area of two MPGDs for low energy (0.1–2 keV) and high-energy (2–10 keV) applications at the focus of XEUS-1 optics. Full colors represent the energy band of X-ray polarimetric sensitivity.

Another interesting possibility would be to use two such detectors optimized for two different range of energy: a low band, 0.1–2 keV, and a high band, 2–10 keV, at the focus of XEUS-1 mirrors. The reduced total time of observation to cover the full energy range would compensate the increase in complexity of the instrument. Fig. 19 shows the effective area of the double instrument, the actual prototype for the high-energy range and an optimized device for the low energy range.

4. Conclusions

The performance obtained with the tested MPGD prototype have demonstrated the great potentiality of this device as photoelectric polarimeter in the 2–10 keV energy band. It produces also high-resolution images ($50\text{--}100 \mu\text{m}$ resolution) and acceptable spectroscopy (16% FWHM at 5.4 keV) at a fast rate (signal duration ~ 30 ns). Moreover, being truly two dimensional, it does not require to be rotated, a clear advantage for space applications. With high throughput optics, as XEUS-1 or SXR mirrors for example, polarimetry of tens of AGN at the % level can be easily done. For all these reasons, the inclusion of a Micropattern Detector in the baseline payload for XEUS-1 is going to be seriously considered.

Acknowledgements

This research is partially funded by Agenzia Spaziale Italiana (ASI).

References

- [1] R.A. Sunyaev, L.G. Titarchuk, *Astron. Astrophys.* 143 (1985) 374.
- [2] M.J. Rees, *Mon. Not. R. Astron. Soc.* 171 (1975) 457.
- [3] N. Gnedin, G.G. Pavlov, Yu.A. Shibano, *Sov. Astron. Lett.* 4 (1978) 117.
- [4] J. Ventura, *Phys. Rev. D* 19 (1979) 1684.
- [5] M.C. Weisskopf, G.G. Cohen, K.S. Long, H.L. Kenstenbaum, R. Novick, R.S. Wolff, *Astrophys. J.* 208 (1976) L125.
- [6] E. Costa, P. Soffitta, R. Bellazzini, A. Brez, N. Lumb, G. Spandre, *Nature* 411 (2001) 662.
- [7] P. Soffitta, E. Costa, G. di Persio, E. Morelli, A. Rubini, R. Bellazzini, A. Brez, R. Raffo, G. Spandre, D. Joy, *Nucl. Instr. and Meth. A* 469 (2001) 164.
- [8] XEUS: information at http://astro.esa.int/SA-general/Projects/XEUS/main/xeus_main.html.